Contents lists available at ScienceDirect

Computers in Biology and Medicine

journal homepage: www.elsevier.com/locate/compbiomed

A comprehensive comparison of various patient-specific CFD models of the left atrium for atrial fibrillation patients

Jorge Dueñas-Pamplona [a,*], Javier García García [a], José Sierra-Pallares [b], Conrado Ferrera [c], Rafael Agujetas [c], José Ramón López-Mínguez [d]

[a] Departamento de Ingeniería Energética, Escuela Técnica Superior de Ingenieros Industriales, Universidad Politécnica de Madrid, C/ José Gutiérrez Abascal 2, Madrid, Spain
[b] Departamento de Ingeniería Energética y Fluidomecánica, Escuela de Ingenieros Industriales, Universidad de Valladolid, C/ Paseo Del Cauce 59, Valladolid, Spain
[c] Departamento de Ingeniería Mecánica, Energética y de Los Materiales, Escuela de Ingenierías Industriales and Instituto de Computación Científica Avanzada (ICCAEX). Universidad de Extremadura, Avda.de Elvas S/n, 06006, Badajoz, Spain
[d] Sección de Cardiología Intervencionista, Servicio de Cardiología, Hospital Universitario de Badajoz, Avda. de Elvas S/n, 06006, Badajoz, Spain

ARTICLE INFO

ABSTRACT

Background: Recently, advances in medical imaging, segmentation techniques, and high-performance computing have supported the use of patient-specific computational fluid dynamics (CFD) simulations. At present, CFD-compatible atrium geometries can be easily reconstructed from atrium images, providing important insight into the atrial fibrillation (AF) phenomenon, and assistance during therapy selection and surgical procedures. However, the hypothesis assumed for such CFD models should be adequately validated.

Aim: This work aims to perform an extensive study of the different hypotheses that are commonly assumed when performing atrial simulations for AF patients, as well as to evaluate and compare the range of indices that are usually applied to assess thrombus formation within the left atrium appendage (LAA).

Methods: The atrial geometries of two AF patients have been segmented. The resulting geometries have been registered and interpolated to construct a dynamic mesh, which has been employed to compare the rigid and flexible models. Two families of hemodynamic indices have been calculated and compared: wall shear-based and blood age distribution-based.

Results: The findings of this study illustrate the importance of validating the rigid atrium hypothesis when utilizing an AF CFD model. In particular, the absence of the A-wave contraction does not avoid a certain degree of passive atrial contraction, making the rigid model a poor approximation in some cases. Moreover, a new thrombosis predicting index has been proposed, i.e., M4, which has been shown to predict stasis more effectively than other indicators.

1. Introduction

Cardiovascular diseases are the leading cause of death worldwide [5]. Thrombus formation inside the blood vessels is the common underlying mechanism of the main cardiovascular diseases (myocardial infarction, ischemic stroke, and venous thromboembolism) [49]. Thromboembolic conditions accounted for 25% of the deaths worldwide in 2010 [49].

The left atrial appendage (LAA) is a prime repository for these thrombi [4]. It is a residual appendix from the left atrium (LA) embryonic development [4], and its high contractility prevents thrombus

formation in healthy patients. Nevertheless, this contractility is significantly reduced in a proportion of the population whose heartbeat is both fast and irregular [6]. This pathology is referred to as atrial fibrillation (AF). It affects 1–2% of adults older than 60 years and more than 10% in patients over 80 years old [7,16,26,28].

LAA's thrombi cause approximately 90% of strokes in patients without valvular AF, and about 60% in patients whose mitral valve (MV) is damaged [4]. The stroke risk in patients with AF increases five-fold compared to healthy patients and seventeen-fold if they also suffer mitral stenosis [50]. For these reasons, the disability and mortality rate is exceptionally high compared to other stroke types [16,26,50]. It leads

to a health expenditure increase estimated at $ 26 billion in the USA. This expenditure is expected to double by 2035 [6]. Clinical and engineering techniques are employed to address the problem and its related costs.

Clinical research is centered on two aspects: morphology analysis and AF treatment. Anatomic treatment has focused on the relationship between the LAA morphology (either its shape [11,48] or its dimensions [19]) and the risk of embolic events. The use of anticoagulants is the preferred treatment. However, physicians usually have to deal with stroke episodes and the appearance of major bleeding, e.g., intracranial and gastrointestinal bleeding [26]. LAA exclusion is a viable alternative [26]. Mechanical enclosure devices are a less invasive method for LAA exclusion [40]. These devices have reduced mortality rates and hemorrhagic and thromboembolic episodes in these patients [29,42,46]. They also serve as a supplement to anticoagulants for stroke recurrence [13].

Advances in medical imaging techniques — such as angiography, transesophageal echocardiography (TEE), and 3D computed tomography (CT) — have allowed cardiologists to gain knowledge for morphology analysis and treatment [27,28]. Moreover, they have paved the way to apply computational fluid dynamics (CFD) techniques to analyze the LA and LAA flow. Zhang and Gay [51] qualitatively demonstrated in an idealized geometry the blood stagnation in the LAA due to AF. The lack of active contraction and high-frequency fibrillation in the LA have a major impact on blood stasis in the LAA [21]. As imaging technology continues to improve, patient-specific geometries studies have also appeared. Flow inside the LA has been characterized [47]. The connection between the risk of stroke and LAA morphology has also been explored [34]. The number of vortexes increases and the flow speed reduces close to the LAA ostium and areas with a higher presence of lobes [34].

CFD can also be a powerful tool for assessing the impact of specific morphological changes. Parametrized LA and LAA have been built to analyze the impact of changes in LA volume, LAA shape, MV, and pulmonary vein (PV) dimensions [14]. PV size growth leads to a lower risk of thrombus appearance. This risk increases as it is in the ostium area. The effect of removing the influence of a patient-specific LA morphology has also been studied [31]. The risk of thrombi appearing does not depend upon the LAA shape's complexity if different LAA geometries are assembled to a common LA geometry. Additional parameters are required to understand the link between this risk and the LAA shape. Other combinations, such as fixing AF conditions in real geometries, have also been approached [6]. In that case, the flow velocity and shear strain rate decrease from the ostium to the LAA tip in healthy patients; this decrease is higher in AF conditions. Furthermore, CFD is so versatile that there have been attempts to model closure devices' presence [2].

These computational works always come to conclusions assuming specific hypotheses (LA wall and boundary conditions) which do not fit with reality. The main one is to set rigid walls for LA, which is the worst AF scenario. This simplification is assumed because it is not possible to obtain the mechanical properties of the endocardium and the different wall layers of the heart. This assumption reduces the capacity to obtain clinical conclusions directly applicable to patients [32]. Hence, it makes more sense to apply dynamic meshes that account for heart wall movement (captured from CT) [30,31,35]. These works segment the 3D LA geometry at a particular instance. They then compute the wall displacement by applying imaging techniques [38,39] to subsequent scans acquired during the cardiac cycle. Finally, they obtain a mesh taking into account the LA wall deformation. These meshes have improved the LAA ostium flow rate calculation [35] and have shown that AF reduces LAA blood purging [30].

Regarding the boundary conditions, it is common practice to employ evenly distributed PV flow, obtained as an estimate. Otani et al. [35] estimated the MV flow rate from variations in ventricle volume. Masci et al. [30] improved these conditions by measuring the MV flow rate, calculating the LA volume variation, and estimating the PV flow rate.

Recently, these authors have applied specific AF conditions by adding a random sinusoidal (4 Hz) displacement to the dynamic mesh.

Nevertheless, these works assume certain hypotheses, such as laminar atrial flow or rigid model, that should be validated. Although some recent works have made an effort to compare rigid and flexible atrium models with patient-specific geometries [15] and perform experimental model validation [12], they still lack patient-specific flow boundary conditions. Our objective is to properly validate these hypotheses on a patient-specific basis, employing patient-specific flow measurements to obtain accurate simulations with clinically relevant conclusions. We will obtain the real LA and LAA geometry of two AF patients and the measured flow for each PV, through TEE, and we will compare flexible and rigid models. Furthermore, we aim to evaluate typical hemodynamic indices based on the wall shear stress (WSS) [14, 21] and the moments of the age distributions [1,25,44].

2. Methods

The workflow of the patient-specific LA blood flow analysis is shown in Fig. 1. It involves data processing of CT images and Doppler TEE, blood flow analysis through patient-specific simulations, and post-processing of the obtained results to study a range of selected thrombosis indices.

2.1. Patient-specific medical data

In this study, CT imaging datasets and Doppler TEE of two patients with a history of AF were used. They were provided by the Cardiology Service of the University Hospital of Badajoz (Spain). The study was approved by the Ethics Committee of the Hospital. All subjects provided written informed consent, per the Declaration of Helsinki.

The first patient (Case 1) experienced paroxysmal AF, with a clinical history of hypertension, and was exhibiting sinus rhythms during data acquisition. For this first patient, only one CT image of the LA endocardial surface was available; therefore, a rigid wall model was employed. Case 1 allowed us to assess the laminar hypothesis for the most critical case since velocities under sinus rhythm are higher than those under fibrillation conditions. In addition, this case was employed to study the influence of different choices of boundary conditions, taking advantage of the Doppler velocity measurements available in the four PVs for this patient. The duration of the cardiac cycle was 0.95s. The second patient (Case 2) suffered from permanent AF and was at fibrillation during data acquisition. Six different CT images in different instants of the cardiac cycle were available so a comparison of the rigid wall assumption against the flexible wall model was performed. Two Doppler-velocity measurements in the PV (left and right) and another in the MV were available, allowing us to perform entire patient-specific simulations under AF conditions. In addition, the last measurement in the MV enabled model validation. More clinical data for both patients are presented in Table 1.

The CT images were acquired using a LightSpeed VCT General Electric Medical Systems (Milwaukee,WI, USA). This scanner is a 64 detector device equipped with snapshot segment mode technology to obtain cardiac images without losing clarity. The scanning parameters were as follows: slice thickness 0.625 mm; rotation time 0.4 s; tube voltage 120 kV; collimation 0.625 mm; and a pitch of 0.18, 0.20, 0.23, or 0.26 (automatically set by the software depending on each patient's heart rate).

TEE with Doppler-based blood velocity measurements were acquired using a Philips EPIC Cvx. The MV and PV curves were recorded. As mentioned, the obtained velocities were employed to establish the simulation boundary conditions and validate the model.

2.2. Left atrium surface segmentation and registration

Manual segmentation is considered the reference, and it is frequently
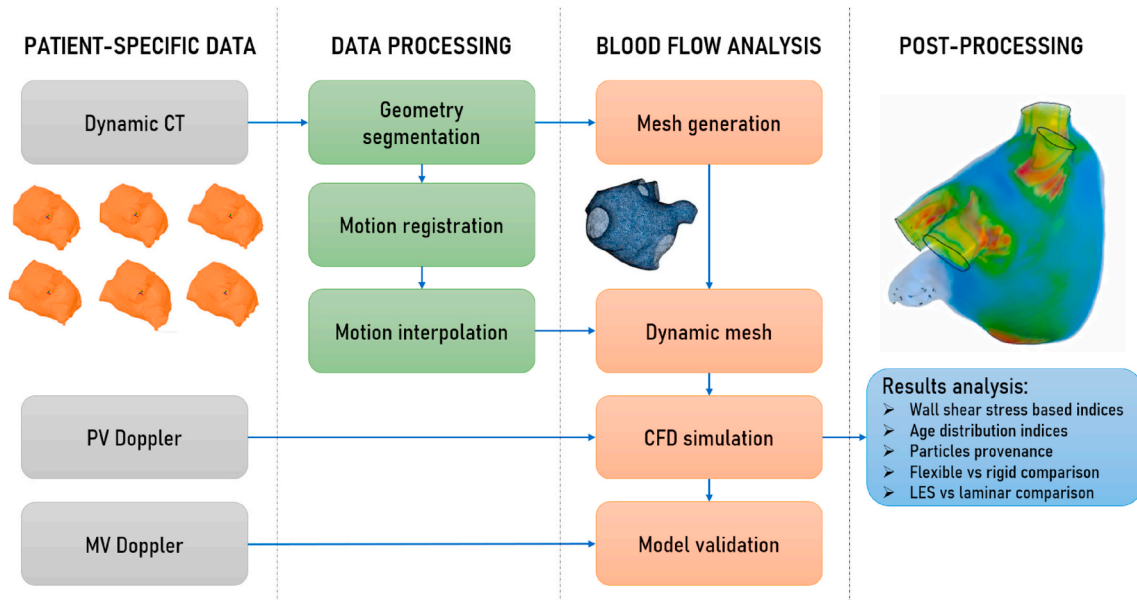
Fig. 1. Workflow of the patient-specific LA blood flow analysis. *Patient-specific data:* the dynamic CT images and MV and PV Doppler TEE were used as the starting point. *Data processing:* the CT images were segmented, registered, and interpolated to reconstruct the LA surface motion through the whole cycle. *Blood flow analysis:* patient-specific simulations were performed with different CFD models both for a rigid and flexible model. *Post-processing:* several indices were selected for study and to compare the obtained results.

Table 1
Clinic data of the patients included in the study.

	Case 1	Case 2
Age [years]	55	82
Sex [Male/Female]	Male	Male
Clinic history	HT/AF	HT/AF/DM/CHD
AF type	Paroxysmal	Permanent
Data acquisition	SR	AF
LA volume [mL]	70–100	141–154
CFG [%]	65	45–50
HR [bpm]	63	50–75
CHA$_2$DS$_2$ − VASc	2	5
HAS-BLED	3	5

SR - Sinus rhythm; HT - hypertension; DM - diabetes mellitus; CHD - coronary heart disease; CFG - cardiac function grading; HR - heart rate.

compared with automatic techniques [8,20]. Nevertheless, semi-automatic segmentation is gaining ground [24] as it offers a perfect balance between manual segmentation (widely used but the slowest) and fully automatic segmentation (fastest but can include numerous wall pixels in the fluid domain). We combined two techniques among the vast number of segmentation algorithms for the heart chambers [37] or specific imaging modalities (CT, MRI) [20]. Two different thresholds were initially selected in the 3D-Slicer software to identify the LA's endocardial surface (including the PV, LAA, and MV). We then added several seeds to these regions and applied the region-growing algorithm to get their geometry. Thresholds, seeds, and their neighborhood were then carefully modified to cover the fluid domain with a mask (171 HU was selected as the minimum threshold and 916 HU as the maximum threshold). Two medical experts, i.e., an interventionist cardiologist and a radiologist, validated the segmentation and carefully analyzed the pixels' intensity level close to the wall in the CT images. Their assessment was very precious as the images' intensity level could change depending on the scanner.

This semi-automatic process is not flawless, and we are aware that a reduced number of pixels belonging to the wall could have been included in the segmented slices. For those cases, the impact of a pixel (300 μm) compared to the LAA ostium diameter (probably the most

critical distance in those geometries), ranges from 1.3 to 1.6%. The impact in the critical area is approximately five times lower than that by a pixel in a stenosed coronary artery (lumen diameter 5 mm and wall thickness 0.5 − 1 mm). Hence, we do not expect flow alterations as in the coronary case [3,41]. Following this procedure, two CFD simulation-compatible 3D models were generated (Fig. 2).

The six CT images available for Case 2 allowed us to reconstruct the cardiac motion throughout the whole cycle. For this purpose, a computational framework similar to that proposed by Otani [35] was used to estimate cardiac motion. The framework is based on the non-rigid registration method — Coherent Point Drift (CPD) — first proposed by Myronenko [33]. This method can compute the 3D displacement fields between the initial mesh (0%RR, where RR indicates the cardiac cycle duration) in all the other deformed meshes so each initial node corresponds to each of the target meshes. This is achieved by solving a probability density estimation problem based on the expectation-maximization algorithm and regularizing the displacement-field to maintain motion coherence. The regularization parameter and span of influence have been set to $\lambda = 10$ and $\beta = 2$ [36].

Subsequently, the four-dimensional (4D) displacement field $u(t)$ of the endocardial LA surface was obtained by interpolating the position of the set of points obtained in the six phases ($i = 1, 2, ..., 6$) from the CPD algorithm. Cubic spline interpolation has been employed to obtain 1000 cardiac phases per cycle, providing a suitable time-step interval for the CFD model.

2.3. Patient-specific left atrial flow simulation

To set up the CFD model, tetrahedral volumetric meshes were generated for both Case 1 and Case 2, using ANSYS® Meshing™ (ANSYS, Inc. Products, Canonsburg, PA, USA). As the large eddy simulation (LES) model is sufficient to detect regions of transitional flow and test the validity of the laminar hypothesis, both laminar and LES model simulations were conducted for Case 1. A mesh convergence study was conducted to confirm that the mesh did not substantially influence the solution. To assess the mesh quality for LES simulation (Case 1), the ratio between subgrid scale turbulent kinetic energy (sgs TKE) and the total turbulent kinetic energy (sum of the former and the resolved TKE) is
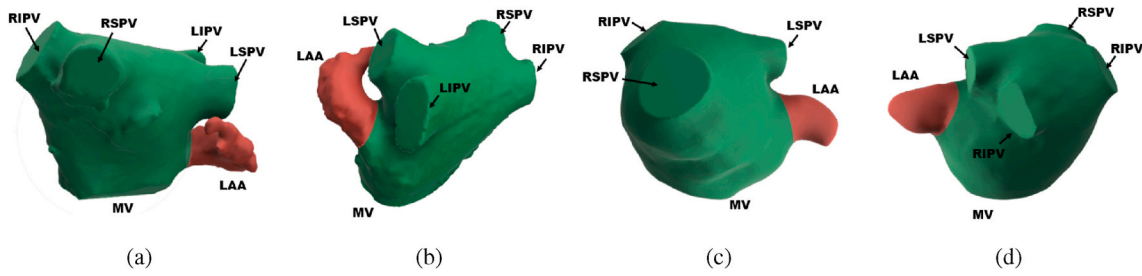
Fig. 2. Patient-specific LA segmented surfaces (posterior and anterior view) for both studied cases. The left atrium is colored in green, while the left atrium appendage is marked in red. (a) Case 1 anterior view, (b) Case 1 posterior view, (c) Case 2 anterior view, and (d) Case 2 posterior view.

used, 90% of cells have a value less than 0.2, meaning that at least 80% of the total kinetic energy is resolved. Regarding the laminar simulations, the flow was validated by performing residual and mesh independence analysis to prove that velocities and pressures have converged and that do not depend on mesh size. As the size cell is not so critical for laminar simulations, a similar level of accuracy was obtained with a significant lower number of cells. The number of cells of the selected meshes was 10370k for Case 1 and 820k for Case 2, with spatial resolutions of 0.5 mm and 5 mm, respectively.

The simulations were performed using the commercial software ANSYS®Fluent 2019R3 (ANSYS, Inc. Products, Canonsburg, PA, USA). Both advection and transient schemes were second-order accurate and convergence criteria of 10^{-4} were used for the residuals. The coupled scheme was selected as the pressure-velocity coupling algorithm for the laminar model. Bounded central differencing for momentum equations and the SIMPLE method for pressure-velocity coupling was selected for the LES model.

As previously mentioned, the atrial motion in Case 2 was preserved by applying ANSYS®Fluent dynamic mesh capabilities. For this purpose, we used an Arbitrary Lagrangian - Eulerian method (ALE) for FSI where the nodes of the computational mesh may be moved with the continuum in normal Lagrangian fashion, or be held fixed in Eulerian manner. Thus, the entire deformation of the left atrium endocardium is imposed at each time step using the results of CT image registration and interpolation. The endocardium velocity is imposed as a Dirichlet boundary condition, in a similar way to Chnafa et al. [9]. The motion of the internal nodes is governed by a modified Laplace equation solved internally by ANSYS Fluent using a smoothing method by employing a node diffusion algorithm, with the cell volume as the diffusion function. The node displacements were small due to the reduced atrial motion; thus, employing remeshing techniques was not necessary in this case.

TEE Doppler measurements provided patient-specific values for the boundary conditions. The measured velocities in the PV were imposed as inlet conditions for both patients and a constant pressure condition equal to zero in the MV. In Case 2, the MV Doppler-velocity was employed to validate the simulation results.

The fluid density and dynamic viscosity were assumed to be $\rho = 1050 kg/m^3$ and $\mu = 0.0035 Pa \cdot s$ respectively [35]. Although red blood cells induce a complex rheological behaviour, for high stress levels and in large vessels, non-Newtonian effects are usually neglected and blood is usually modelled as an incompressible Newtonian fluid in numerical simulations of the LA and LAA flows [6,9,35]. For this reason, blood was assumed to be a Newtonian fluid. The flow was computed by solving the continuity and Navier-Stokes equations (Equations (1) and (2) respectively) where **v** is the velocity vector and p is the pressure,

$$\nabla \cdot \mathbf{v} = 0 \tag{1}$$

$$\frac{\partial \mathbf{v}}{\partial t} + \mathbf{v} \cdot \nabla \mathbf{v} = -\frac{\nabla p}{\rho} + \frac{\mu}{\rho} \nabla^2 \mathbf{v} \tag{2}$$

The time-step was equal to 0.001s for both cases. A time convergence analysis was performed, demonstrating that the simulation loses

memory of the initial condition from the fourth cycle on. Therefore, the performed analysis is based on the results beyond the fourth cycle. For LES simulation, we obtained that for the next cardiac cycles the phase averaged fluctuating velocities changed less than 5% [9], therefore we considered that the solution was statistically stable and during the next 15 cardiac cycles we made a phase average of the variables. The results presented in the paper regarding LES simulation correspond to these phase averaged values.

2.4. Hemodynamic indices

Various indices have been employed to assess LAA flow and the probability of thrombus formation. Two families of hemodynamic indices were calculated: indices associated with wall shear stress based distribution, e.g., time-averaged wall shear stress (TAWSS), oscillatory shear index (OSI), endothelial cell activation potential (ECAP), and relative residence time (RRT); and indices related to stasis, e.g., the moments of age distribution [43] and scalar transport of related tracers.

2.4.1. Age distribution associated indices

In this work, a residence time analysis based on the age of the fluid was performed. Usually, the age of the fluid is computed in cardiac flow to detect stasis and locate areas prone to thrombi formation because of relatively high residence times. In this case, we extend the analysis using the moment generation equation of Sierra-Pallares et al. [43] to compute the mean age of the blood and related moments of age, which supply additional information. Following Sierra-Pallares et al. [43], the moment generation equation for a laminar flow of a non-reactive tracer is

$$\frac{\partial}{\partial t}(\rho \xi m_k) + \nabla \cdot (\rho \mathbf{v} \xi m_k) = \nabla \cdot \left[\Gamma_{m_k} \nabla(\xi m_k) \right] + \rho k \xi m_{k-1} \tag{3}$$

where m_k is the k moment of the age distribution, ξ is the mixture fraction, Γ_{m_k} is the mass diffusivity of the moment m_k, and **v** is the velocity. This equation allows us to compute the moments of the age distribution of the blood entering for each PV. We fixed $\xi = 1$ for the entire computational domain; in this case, we are not interested in knowing the mean age of the blood flowing from a particular inlet but the global range. Thus, the equation is reduced to:

$$\frac{\partial}{\partial t}(\rho m_k) + \nabla \cdot (\rho \mathbf{v} m_k) = \nabla \cdot \left[\Gamma_{m_k} \nabla(m_k) \right] + \rho k m_{k-1} \tag{4}$$

which corresponds to the moment of age equations derived elsewhere [25,44]. Through the above hypothesis, it can be proven that $m_0 = 1$ [43]. With the set of equation (4), it is possible to solve for the required moment of age. In this work, we solve for m_1 to m_4 to compute the following quantities:

- The mean age of the fluid ($a = m_1$) is the first moment of the distribution function. This indicates the amount of time the tracer needs to reach some point in the computational domain. High a values

should indicate stasis, although this metric does not straightforwardly indentify stagnant zones.

- The washout (φ) was calculated by solving its scalar transport equation. At the beginning of the fourth cycle, φ was set to one for the entire calculation domain. Subsequently, the incoming flow has a value of $\varphi = 0$ and thus the washout was calculated as the residual value of φ within the LAA during the following cycles.
- An index based on a normalized fourth moment, defined as M4 $= \frac{m_4}{\sigma^2}$, where $\sigma = m_2 - m_1^2$. In areas where the mean age is large, the fourth moment is even larger and it provides a better picture of stagnant zones than the mean age. We normalized the fourth moment with the age variance to produce a non-dimensional number.

2.4.2. Wall shear stress based indices

Several indices derived from wall shear stress are commonly associated with blood stasis and higher coagulation risks, such as TAWSS, OSI, ECAP, and RRT [10,22,45]. The definitions of this four indices can be found in Table 2. Recent studies have employed these indices for atrial simulation, relating them to coagulation risk in the LAA [2,34].

- TAWSS represents the mechanobiological effect of wall shear stress in the LAA wall during the entire cardiac cycle. Low values of TAWSS represent low flow velocities, which are related to thrombus formation in the LAA.
- OSI is a non-dimensional parameter that has also proven to be successful in identifying the atheroprone region [22]. The OSI captures the flow oscillation in both magnitude and direction by comparing the wall shear stress mean with its magnitude. The values range between 0 for a constant flow and 0.5 when the flow direction is completely inverted during the cardiac cycle.
- The ECAP index is associated with endothelial susceptibility, which leads to an increase in thrombus formation risk [10]. It considers both the TAWSS and OSI indices; hence, the regions exposed to both high OSI and low TAWSS have high ECAP values.
- RRT combines wall shear stress and OSI to capture the residence time of blood particles near the atrium wall. This is related to platelet aggregation in the endothelium [17,18,45].

2.4.3. Colored particles

In Case 2, a colored particle analysis was performed to determine the provenance of the fluid particles reaching the LAA. For this purpose, the particles coming from each PV were marked with different colors: red for the right superior, blue for the right inferior, green for the left superior, and yellow for the left inferior. The particle distribution in the LAA was studied to confirm which PV has more influence over LAA flow.

Table 2
Thrombi formation indices analyzed in this work.

Age distribution-based indices	
Mean age	m_1
Washout	φ
M4	m_4/σ^2
Wall shear stress based indices	
TAWSS	$\frac{1}{T}\int_0^T |WSS| dt$
OSI	$\frac{1}{2}\left(1 - \frac{\left|\int_0^T WSS\, dt\right|}{\int_0^T |WSS|\, dt}\right)$
ECAP	OSI/TAWSS
RRT	$[(1 - 2{\cdot}OSI){\cdot}TAWSS]^{-1}$

3. Results

3.1. Comparison between LES and laminar model - case 1

A transient rigid wall simulation was launched to compare laminar and LES models (Case 1). The four measured PV Doppler velocities were imposed as inlet boundary conditions. Fig. 3a shows the agreement between the LES and laminar models for the MV velocity. Fig. 3b shows a volume rendering of the eddy viscosity ratio for the LES model in the cycle instant of maximum velocity (14%RR) while Fig. 3c shows the residence time for the laminar model at the end of the fifth cycle (100%RR).

Figs. 4 and 5 show the volume renderings of the simulation results, comparing the laminar and LES models. Fig. 4 shows the velocity magnitude for three instants during the last simulated cycle: 14%RR, 44%RR, and 84%RR. The first instant represents the peak cycle velocity (14%RR); the second represents mid-cycle, with the flow still coming into the LA (44%RR); and the last represents the instant of minimum velocity in the cycle (84%RR). The first column in the figure represents the results of the laminar model while the second column represents the LES model. The lowest velocities are found in the LAA for all cycle instants, as it was expected. We can observe that there are no relevant differences between both models, suggesting that the laminar flow was preserved through the entire cardiac cycle. The same disposition is presented in Fig. 5, where the second invariant Q of the velocity gradient is displayed. This Q-criterion is a commonly employed method for detecting and visualizing vortex structures; here, the value of $Q = 0.05s^{-2}$ has been used as a reference. As there cannot be seen significant differences in the Q-isosurfaces between both models, this suggests that there are not turbulent fluctuations.

3.2. PV boundary conditions analysis - case 1

Case 1 geometry and patient-specific boundary conditions were also employed to study the existence of symmetry between the flow profiles in the PV. This analysis is crucial to assist simulations in which the information for the four PVs is not available. Following this idea, four different boundary condition combinations in the PV were studied with the laminar model. The simulation results were compared to determine the relative degree of similarity. We start with the best scenario, when all velocity Doppler profiles are available. In this simulation, a different velocity profile is imposed in each vein. Subsequently, we employ only two different velocity profiles: the first belongs to the right PV and the second to the left PV. Finally, the third and fourth cases correspond to those when only one velocity profile is available (right and left, respectively). A comparison of the MV flow for these four different boundary condition cases is shown in Fig. 3d and will be discussed in the next section.

3.3. Comparison between rigid and flexible atrium model - case 2

Regarding Case 2, we took advantage of the hypotheses tested and confirmed in Case 1. Therefore, we assumed laminar flow and symmetry between the PV on the same side. Following this strategy, the measured right profile was imposed as a boundary condition on both the right PVs and the left profile for the left PV.

The Case 2 patient suffered severe AF and atrial motion exhibited a significant reduction. Six geometries corresponding to different instants of the cycle provided by the hospital allowed us to test if there was an appreciable difference between a rigid and flexible simulation in such cases. Both rigid-wall and flexible simulations were conducted for comparison. The volume variation through the cycle is shown in Fig. 6a: orange points represent the volume of the six segmented geometries while the volume variation of the interpolated geometries is depicted by the blue line. It can be seen that the volume variation throughout the
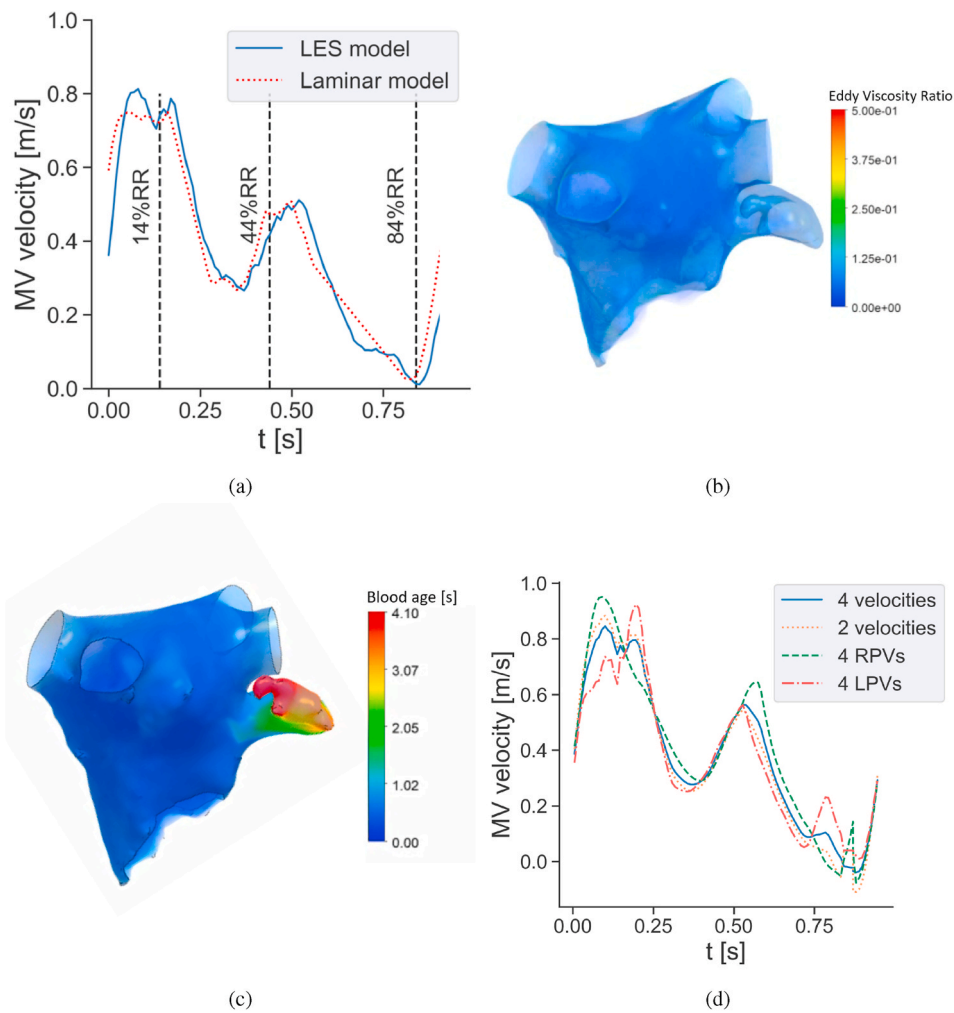
Fig. 3. Rigid wall simulation results (Case 1). (a) Comparison between the MV velocities obtained from the laminar and LES models respectively, (b) eddy viscosity ratio for the LES model (14%RR), (c) residence time for the laminar model at the end of the fifth cycle, and (d) comparison between the four different boundary condition scenarios: 4 different measured PV, symmetric flow between the right and left PV, all right PV and all left PV.

entire cycle is lower than 5%. The flows in the PV (measured and imposed) and in the MV (from simulation) are depicted in Fig. 6b, where the atrial volume variation through the cycle is displayed as well.

Fig. 6c plots the comparison of the measured MV velocity with the velocities obtained for both the flexible and rigid model. As it will be discussed in the next section, a very reasonable agreement was found between them, supporting the use of TEE Doppler patient-specific boundary conditions and allowing us to validate the model.

In addition, as mentioned in Section 2.4.3, a colored particle analysis was performed to study the provenance of the fluid that finally reaches the LAA (Fig. 7). The fraction of particles coming from each PV at the end of the cycle was the following: 64.7% (RSPV), 18.4% (RIPV), 13.2% (LSPV), and 3.7% (LIPV). This particle distribution can be useful for confirming the hypothesis that the LAA flow is more influenced by the right PVs than the left PVs.

3.4. Comparison between different hemodynamic indices - case 2

As stated in Section 2.4, different hemodynamic indices were calculated and compared for both models: shear indices and age distribution indices. The first two columns of Fig. 8 compare TAWSS, OSI, ECAP, and RRT indices within the LAA, for both rigid and flexible models. The third column shows the probability density function (PDF) comparison of both models. All of them were calculated based on the wall shear stress, averaged over the last simulated cycle.

Age distribution-based hemodynamic indices are compared in Fig. 9, i.e., washout, age of fluid, and M4. The iso-surfaces results for the first four cycles are presented in the first column, with the latter being the PDF comparison between the rigid and flexible model through the last four cycles. The values selected to represent the iso-surfaces are 0.1, 0.2, 0.3, and 0.4 for the washout, 1 s, 2 s, 3 s and 4 s for the blood age, and 2500, 5000, 7500, and 10000 for M4. In the Figure it can be seen the evolution of the age distribution-based indices, addressing cumulative differences per cycle between both models. For both cases the most critical points are located at the tip of the LAA: the difference between these results and the ones obtained with the wall shear stress based indices will be thoroughly discussed in the next section.

4. Discussion

This work aims to deepen existing knowledge regarding CFD models of the LA under AF conditions and verifying some of the hypotheses that are commonly assumed in previous works. It is common to assume laminar flow [2,6,21,31,35] and the rigid atrium hypothesis under AF conditions [2,6,14,31,51]. Although some studies have already performed flexible simulations to study LAA flow [15,21,35], more work is required to establish in which cases the rigid LA hypothesis can be considered valid. For this purpose, LA CT-geometries of the two AF patients were segmented and meshed to perform computational fluid simulations, as mentioned in Section 2. Case 1 was used to check the
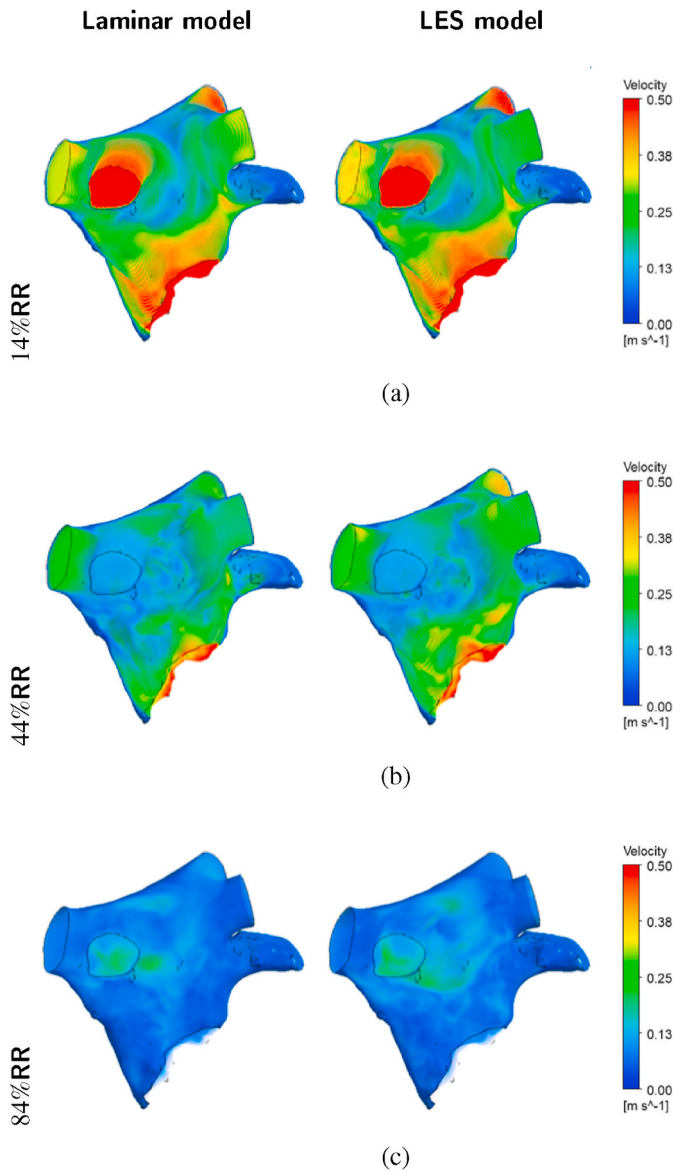
Laminar model   **LES model**

(a)

(b)

(c)

Fig. 4. Velocity magnitude rendering in three specific instants (Case 1): 14%RR, 44%RR, and 84%RR. The first column represents the laminar model and the second the LES model.
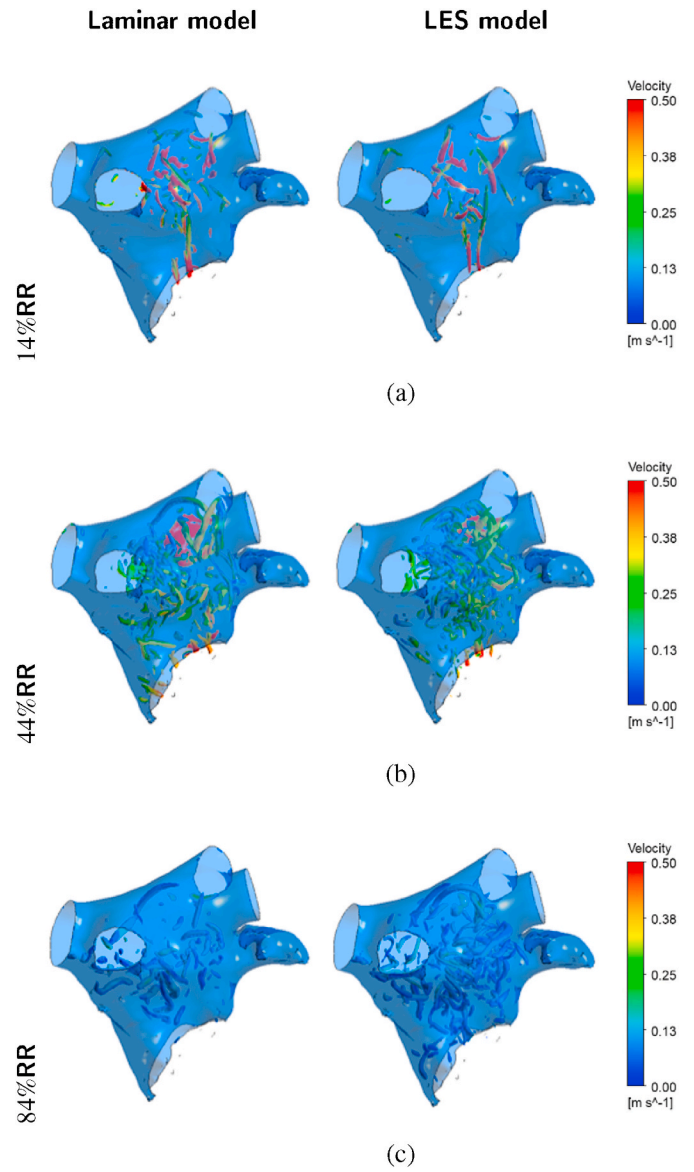
Laminar model   **LES model**

(a)

(b)

(c)

Fig. 5. Isosurfaces representation for $Q = 0.05s^{-2}$ in three cycle instants (Case 1): 14%RR, 44%RR, and 84%RR. The first column represents the laminar model and the second the LES model.

laminar hypothesis and perform an analysis of the flow symmetries between the PV inflows, while Case 2 was used to perform a comparison between rigid and flexible models in a patient with severe AF. Subsequently, the results for both the rigid and flexible models of Case 2 were compared for the different hemodynamic indices. These indices provide relevant information concerning locations where the thrombus is more prone to form inside the LAA. The comparison can also elucidate which geometries are more prone to thrombus formation in the future.

4.1. Comparison between LES and laminar model - case 1

Regarding the comparison between the laminar and LES models, little difference can be seen in the MV velocity between both models (Fig. 3a). The eddy viscosity ratio is below 0.2 in the cycle instant of maximum velocity (Fig. 3b, 14%RR), indicating that there are not significant turbulent fluctuations. Therefore the flow can be considered as laminar throughout the whole cardiac cycle. This is in accordance with previous "in vivo" evidence [48] and simulation works [2,6,21,31,35]. The high blood age observed at the end of the last cycle (Fig. 3c) shows

the poor wash of the LAA by LA flow, which increases the probability of thrombus formation during an AF episode [11,19,29]. The results of the PV boundary conditions analysis in the MV valve velocity (Fig. 3d) allow us to infer some degree of symmetry in the flow between the left and right PV, which is in accordance with previous results [23]. The case with four different PV velocities does not present a significant difference from the case with only two different velocities (one right and one left). The cases where the velocities are all four right PVs or all four left PVs do not differ much from previous cases, although the difference is more marked. Considering the above results can be very useful in cases when the boundary condition information for the 4 PV are not available.

The lowest velocities were found in the LAA for all cycle instants (Fig. 4); therefore, Case 1 was prone to thrombus formation in that location [11]. Even during the instant 14%RR (which represents the peak cycle velocity), the LAA velocities remained very low. This was due to a combination of various mechanical and geometric factors [29], i.e., the rigidity of the LA and LAA, their geometry and disposition, the angle of the PV, the magnitude of the cardiac output, etc. It is important to emphasize that this does not imply that this patient must be
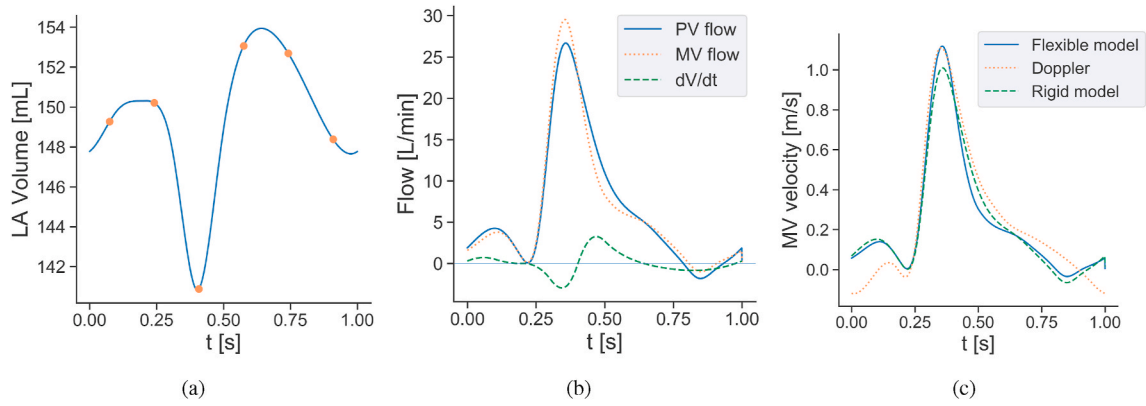
Fig. 6. Volume and flow boundary conditions, models comparison, and validation (Case 2): (a) Left atrial volume temporal evolution. The volume of the six segmented geometries is marked with orange points while the blue line represents the volume variation of the interpolated geometries, (b) PV and MV flows and volume temporal evolution, and (c) MV velocity comparison between the laminar rigid model, the flexible model, and the measured Doppler-velocities.
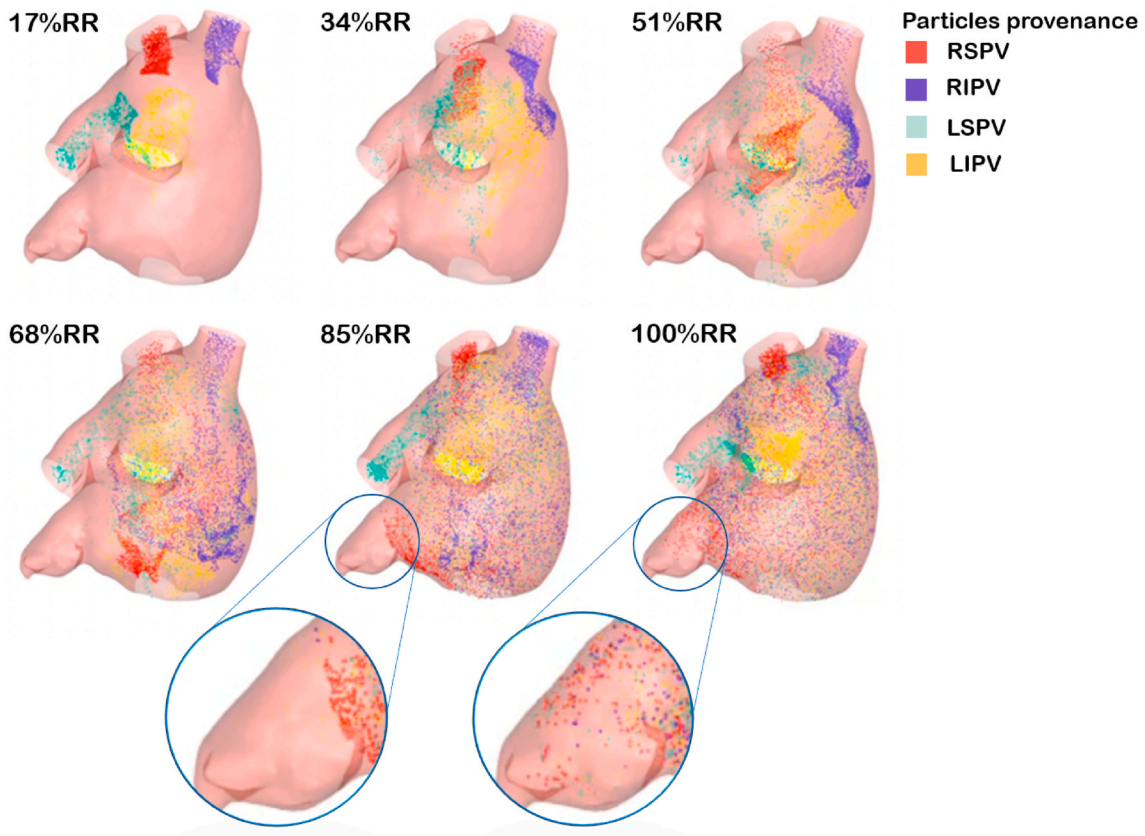

Fig. 7. Evolution of the colored particles for six different cycle instants (Case 2, rigid model). The fraction of particles coming from each PV at the end of the cycle was the following: 64.7% (RSPV), 18.4% (RIPV), 13.2% (LSPV) and 3.7% (LIPV).

experiencing a thrombus process but it does indicate that the mechanical factors give a higher probability of thrombus formation.

As there cannot be seen significant differences in the Q-isosurfaces (Fig. 5) between both models this confirmed the laminar flow; this assumption was directly applied to Case 2.

4.2. Comparison between rigid and flexible atrium model - case 2

In Case 2, the registered atrium wall presented a small but significant volume variation (Fig. 6a) of no more than 5%, which was small enough to test the rigid wall assumption [6,14]. The LA had completely lost its A-wave (due to active contraction) so the atrial contraction shown in the

figure is fully passive because of the suction effect generated after the MV opening [51]. According to the principle of mass continuity, this difference between atrial inflow and outflow must be equal to the atrial volume variation, as is the case (Fig. 6b). A remarkable agreement was found between the MV velocity obtained with the flexible model and that measured by the Doppler-effect (Fig. 6c), so the model can be considered as validated. The agreement achieved between the simulated and measured MV velocities remarks the benefits of employing patient-specific TEE Doppler measurements as boundary conditions. The rigid model, although not far from the flexible model, appears to be a worse approximation in this case. This is in accordance with other recent works [15], which also caution the use of the rigid wall hypothesis.
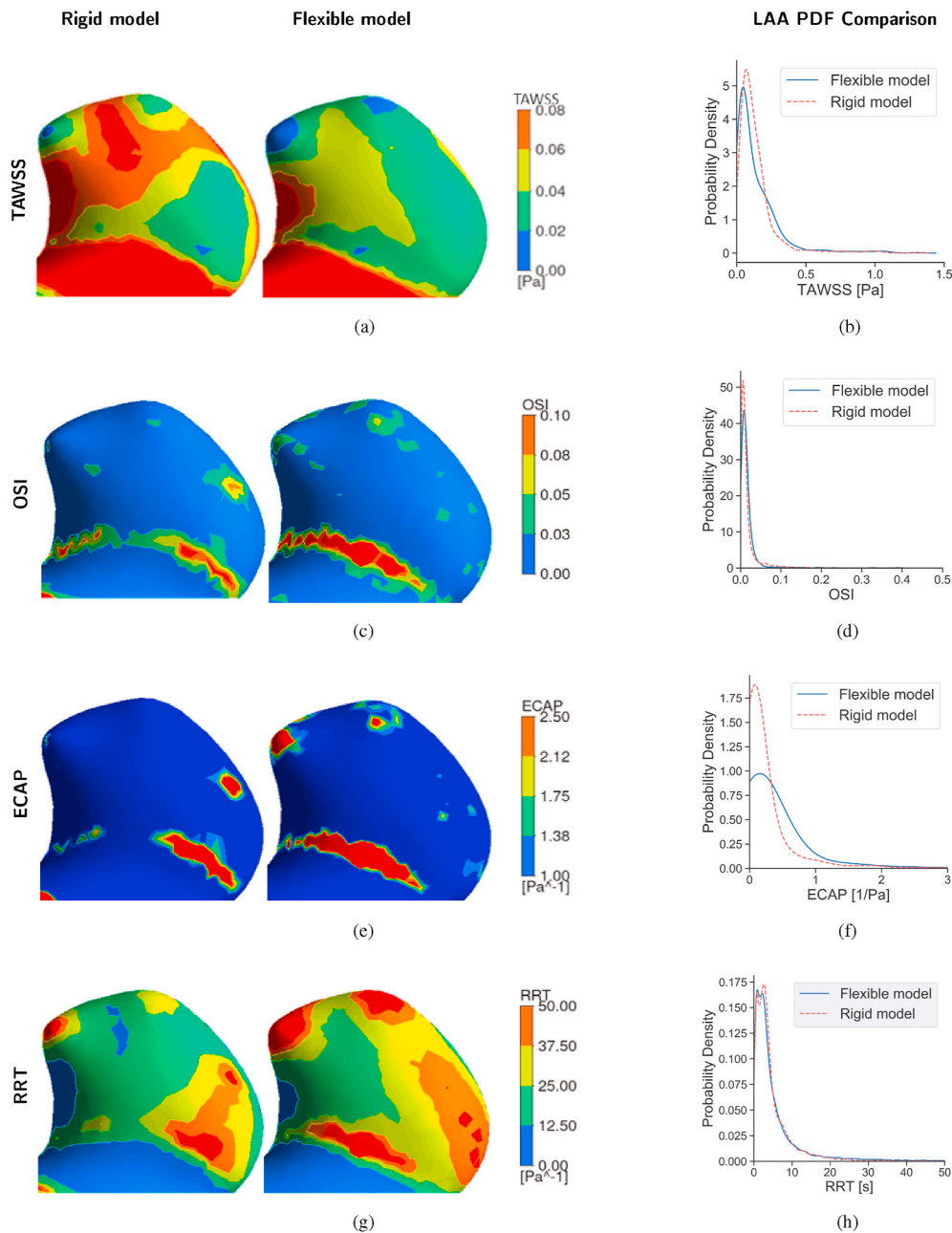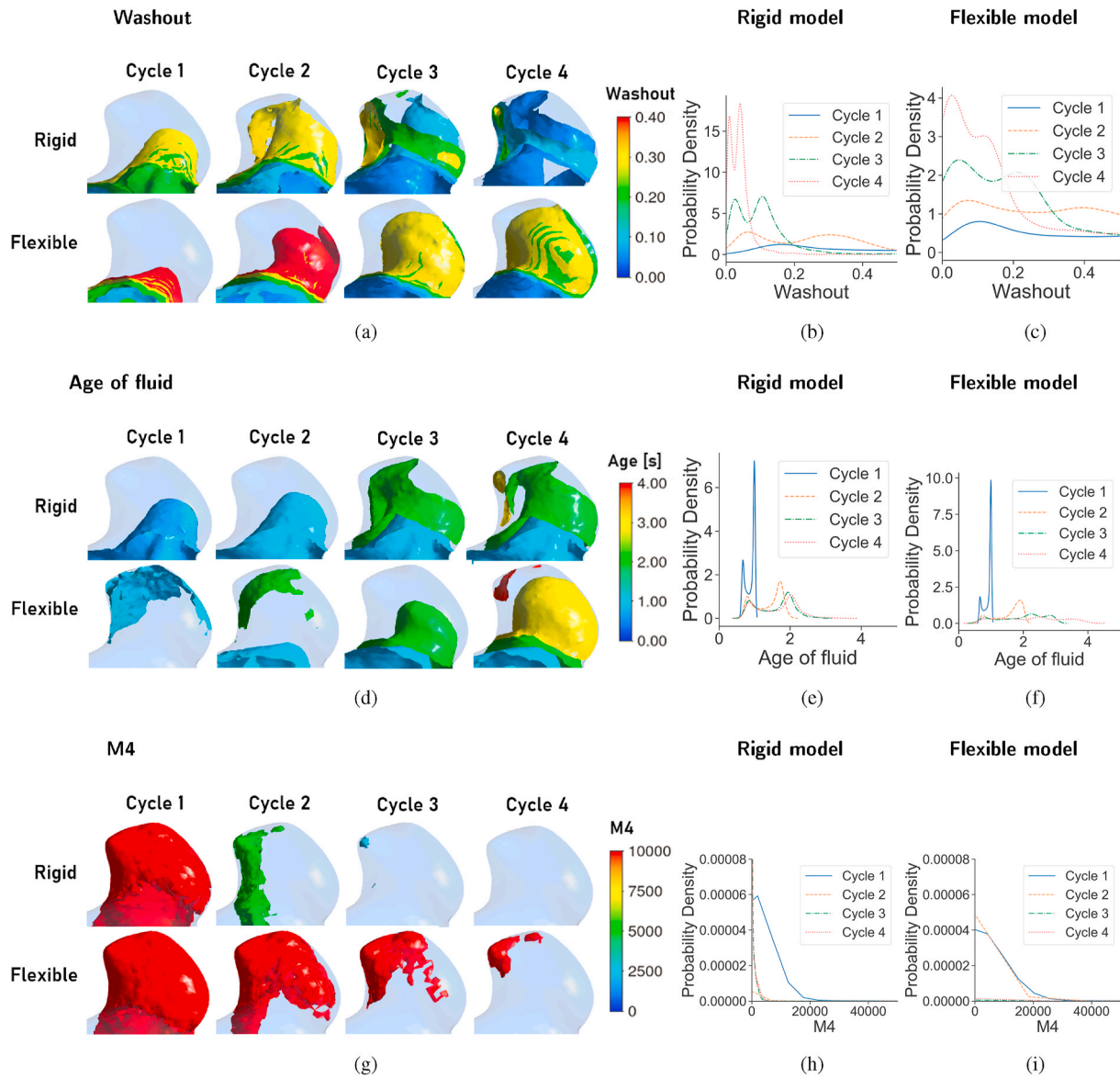
Fig. 8. LAA model results for the rigid and flexible model (Case 2), comparing the wall shear-based hemodynamic indices: (a-b) TAWSS, (c-d) OSI, (e-f) ECAP, and (g-h) RRT. The first and second columns show the contour results for the rigid and flexible model, respectively. The third column presents a PDF comparison between both models.

Concerning the colored particle analysis, the fraction of particles coming from the right PVs was 83.1%. This confirms that the LAA flow is more influenced by the right PVs and the left PVs have a minor impact, which is consistent with results found in previous studies [35]. The particle analysis can be seen in Fig. 7.

In the previous section, two families of hemodynamic indices were calculated and compared for Case 2: wall shear-based indices and moment distribution based indices. LAA TAWSS contours (Fig. 8a) allow us to infer that, in this case, the LAA velocities and thus the washing effect is higher for the rigid case. Even though the TAWSS contour distributions are quite similar between both cases, the values are still lower in the flexible case. This is explained by the fact that, in cases where the atrial contraction is drastically reduced, the rigid model is not necessarily the most critical from the perspective of thrombosis risk. In any case, the results between both models should be similar due to the

pathology [2,51]. This would not be so for a healthy atrium where the flexible and rigid models should differ greatly. The same tendency is followed by the OSI (Fig. 8d). OSI represents the direction change of the wall shear stress vector from a predominant blood flow direction during the cardiac cycle. The calculated values are not very high (being a maximum of 0.1) so the flow does not experience strong directional changes within the LAA [22]. We can notice a difference in the tip where the appendage ends in the ECAP distribution (Fig. 8f). The flexible model detected two critical zones that were not detected by the rigid model: the existing differences between the models for the TAWSS and the OSI values were combined to create an effective difference in this zone. A similar result occurred for the last indicator, the RRT (Fig. 8h); the tip of the appendage was marked as critical by the flexible model in nearly the same zones as the ECAP [18]. The PDF (Fig. 8, third column) showed and quantitatively confirmed the same conclusions that we have

Fig. 9. LAA model results for the rigid and flexible model (Case 2), comparing the age distribution based hemodynamic indices: (a-c) washout, (d-f) age of fluid, and (g-i) M4. The first column shows the isosurfaces for the last four cycles and the last two columns present a PDF comparison between both models and the evolution through the different cycles.

just obtained from the wall contours.

All of the age moment distribution indices seemed to address cumulative differences per cycle between both models. Washout was higher for the rigid case (Fig. 9a) as the fluid within the LAA was reinvigorated faster than for the flexible case. The blood age in the fourth cycle shows that there is a lack of new blood entering the LAA, which causes a blood stagnation within the appendage, increasing the risk of thrombus formation [51]. As expected, the flexible model predicts a higher age, in accordance with previous results. The highest age found in the LAA was higher in the flexible model than in the rigid one. In both cases, the most critical points are located at the tip of the LAA. It must be emphasized that the blood age value depends upon the number of simulated cycles so is a relative index. This is a key reason for employing M4 as a thrombosis index, as it is non-dimensional and effectively filters out the zones with lower ages.

Finally, the M4 index tends to rise quickly, reaching high values in the earlier cycles (Fig. 9g); it then tends to disappear in the subsequent cycles, as can be seen in the rigid model. Hence, the M4 index has the advantage of predicting stasis at earlier simulation times than other

indices, visibly defining the most critical zone. It is worth noting that, although both families of indices indicate the more prothrombotic zones in the LAA, the shear-based and distribution-based indices do not indicate the same zones; this is because the moment distribution indices focus on the zone with higher blood age and thus the lowest velocities in the LAA (at the tip of the appendage). Conversely, both the ECAP and the RRT not only mark the zones with the lowest velocities but also the zones where there are rapid changes in velocity [2,14] (detected by the OSI index); this explains why the ECAP and the RRT, in this case, have marked a narrow band near the ostium (which is the region of changing velocities), as well as the appendage tip. At present, it remains unclear which of these mechanisms is more critical for the thrombus formation process in the LAA and whether the higher residence time or the rapid velocity direction changes near the ostium. More work is required in this direction to deepen existing knowledge regarding thrombus formation within the LAA.

4.3. Clinical aplications

The usefulness of CFD to assist cardiac diagnosis has been strongly proven by several studies and has become a crucial tool for achieving a better understanding of the LAA thrombosis process and numerically quantifying thrombosis risk on a patient-specific basis [15,21,31,35]. This has allowed the scientific community to develop tools for identifying patient groups, selecting the optimum therapy, or even assisting clinicians during surgical procedures. Several recent works present numerical analyses of LA flow patterns, some of them including the LAA and assuming AF conditions. These studies have provided important insights into the AF phenomenon and to calculate otherwise inaccessible parameters related to thrombus formation, such as residence times, vorticities, and shear stresses. Nevertheless, their common weakness seems to be the difficulty in selecting accurate patient-specific boundary conditions, selecting the correct numerical model hypotheses, and performing model validation. This may lead to questioning of the findings obtained through numerical simulation, drawing attention to the need for an accurate atrial model with physiological conditions to be developed and the corresponding hypotheses to be validated, which is precisely the aim of this work.

The methodology proposed in this work may be used to perform accurate atrium simulations and its validation, using the simulation-derived metrics proposed here as a reference to measure the thrombosis risk. As for routine clinical use, such decision support systems need to be computationally inexpensive; digital twins and machine learning will play an important role in this field, which will be explored in our future work.

4.4. Limitations

More cases are needed to confirm and generalize the obtained results. Unfortunately, no more geometries were available to the authors and so this study is restricted to the cases presented herein. Future work will focus on extending this study to more patients and furthering the study of different hemodynamic parameters. It is fundamental to establish a condition to indicate in which cases the rigid atrium hypothesis is valid on a patient-specific basis.

It should be noted that the accuracy of motion estimation techniques using non-rigid registration highly depends on the spatio-temporal resolution and the image quality of the CT images. Herein, the CT resolution has been considered good enough to reproduce the main characteristics of the flow inside the LA and its corresponding influence on the LAA. The pitch (300micro meter) ranges from 0.18 to 0.26 and the impact of a pixel compared to the LAA ostium diameter (probably the most critical distance in this study), ranges from 1.3 to 1.6%.

Blood is a non-Newtonian fluid with shear-thinning properties, as red blood cells induce a complex rheological behaviour. However, for high stress levels and in large vessels, non-Newtonian effects are usually neglected and blood is usually modelled as an incompressible Newtonian fluid in numerical simulations of the LA and LAA flows [9,35]. We have considered this hypothesis as acceptable in this work.

In our analysis we do not have considered the secondary flow that can occur when the primary flow follows a curved path, because the available TEE Doppler measurements only give the velocity evolution trough the cardiac cycle at a specific point. However, despite this uncertainty, the level of turbulence obtained is so low that it is not expected that the inclusion of the secondary flow will significantly affect the results.

Biochemical modeling of thrombus formation could be incorporated into the atrial model. However, whether this will considerably increase simulation time and accuracy when applied to patient-specific models is still unclear.

5. Conclusion

This study has combined the use of patient-specific atrial geometries and their motions with PV and MV Doppler-velocities to perform simulations in fibrillation conditions with complete patient-specific boundary conditions, which, to the best of our knowledge, has not yet been accomplished before.

In addition, some commonly employed hypotheses when performing CFD atrial simulations have been tested. The laminar hypothesis was validated by comparing the laminar and LES models and studying the turbulence patterns. The rigid atrium hypothesis has been tested, drawing attention to the necessity of validating this hypothesis before its application; the rigid model is not more thrombogenic than the flexible model for all patient-specific atrium geometries. A major cause of this is the complex nature of atrial flow: a certain degree of passive atrial contraction may remain in patients with no active atrial contraction. However, rigid simulations could remain as a useful indicator to assess the thrombotic risk of a patient-specific geometry, as they only require static images that are commonly employed in clinical practice. To our knowledge, a unified criterion does not yet exist for when the rigid atrium hypothesis should be applied; thus, more work is required in this direction.

Furthermore, a range of different existing models and hemodynamic indices have been calculated and compared, showing interesting differences between the wall shear-based and moment-distribution-based indices. A new index has been proposed: the M4 index has been shown to predict the formation of pro-thrombotic areas more effectively than the other indices.

Declaration of competing interest

The authors declare no conflict of interest.

References

[1] J.T. Adeosun, A. Lawal, Residence-time distribution as a measure of mixing in t-junction and multilaminated/elongational flow micromixers, Chem. Eng. Sci. 65 (2010) 1865–1874.

[2] A.M. Aguado, A.L. Olivares, C. Yagüe, E. Silva, M. Nuñez-Garciá, Á. Fernandez-Quilez, J. Mill, I. Genua, D. Arzamendi, T. De Potter, X. Freixa, O. Camara, In silico optimization of left atrial appendage Occluder implantation using interactive and modeling tools, Front. Physiol. 10 (2019) 1–13, https://doi.org/10.3389/fphys.2019.00237.

[3] R. Agujetas, M.R. González-Fernández, J.M. Nogales-Asensio, J.M. Montanero, Numerical analysis of the pressure drop across highly-eccentric coronary stenoses: application to the calculation of the fractional flow reserve, Biomed. Eng. Online 17 (2018) 67.

[4] N.M. Al-Saady, O.A. Obel, A.J. Camm, Left atrial appendage: structure, function, and role in thromboembolism, Heart 82 (1999) 547–554, https://doi.org/10.1136/hrt.82.5.547.

[5] E.J. Benjamin, et al., Heart disease and stroke statistics'2017 update: a report from the american heart association, Circulation 135 (2017) e146–e603, https://doi.org/10.1161/CIR.0000000000000485.

[6] G.M. Bosi, A. Cook, R. Rai, L.J. Menezes, S. Schievano, R. Torii, G. Burriesci, Computational fluid dynamic analysis of the left atrial appendage to predict thrombosis risk, Front. Cardiovasc. Med. 5 (2018) 1–8, https://doi.org/10.3389/fcvm.2018.00034.

[7] L. Cea-Calvo, J. Redón, J.V. Lozano, C. Fernández-Pérez, J.C. Martí-Canales, J. L. Llisterri, J. González-Esteban, J. Aznar, Prevalencia de fibrilación auricular en la población Española de 60 o más años de edad. Estudio PREV-ICTUS, Rev. Esp. Cardiol. 60 (2007) 616–624, https://doi.org/10.1157/13107118.

[8] C. Chen, C. Qin, H. Qiu, G. Tarroni, J. Duan, W. Bai, D. Rueckert, Deep learning for cardiac image segmentation: a review, Front. Cardiovasc. Med. 7 (2020) 25, https://doi.org/10.3389/fcvm.2020.00025.

[9] C. Chnafa, S. Mendez, F. Nicoud, Image-based large-eddy simulation in a realistic left heart, Comput. Fluids 94 (2014) 173–187.

[10] P. Di Achille, G. Tellides, C. Figueroa, J. Humphrey, A haemodynamic predictor of intraluminal thrombus formation in abdominal aortic aneurysms, Proc. Math. Phys. Eng. Sci. 470 (2014) 20140163.

[11] L. Di Biase, P. Santangeli, M. Anselmino, P. Mohanty, I. Salvetti, S. Gili, R. Horton, J.E. Sanchez, R. Bai, S. Mohanty, A. Pump, M. Cereceda Brantes, G.J. Gallinghouse, J.D. Burkhardt, F. Cesarani, M. Scaglione, A. Natale, F. Gaita, Does the left atrial appendage morphology correlate with the risk of stroke in patients with atrial fibrillation? Results from a multicenter study, J. Am. Coll. Cardiol. 60 (2012) 531–538, https://doi.org/10.1016/j.jacc.2012.04.032. URL.

[12] J. Dueñas-Pamplona, J. Sierra-Pallares, J. García, F. Castro, J. Muñoz-Paniagua, Boundary-condition analysis of an idealized left atrium model, Ann. Biomed. Eng. (2021), https://doi.org/10.1007/s10439-020-02702-x.

[13] X. Freixa, I. Cruz-González, A. Regueiro, L. Nombela-Franco, R. Estévez-Loureiro, R. Ruiz-Salmerón, A. Bethencourt, H. Gutiérrez-García, J.A. Fernández-Díaz, J. C. Moreno-Samos, P. Jiménez-Quevedo, V. Martin-Yuste, R. Arnold, X. Millan, L. Asmarats, M. Ronquillo, V.H. Agudelo-Montañez, J.R. López-Mínguez, J. Goicolea, A.P. De Prado, D. Arzamendi, Left atrial appendage occlusion as adjunctive therapy to anticoagulation for stroke recurrence, J. Invasive Cardiol. 31 (2019) 212–216.

[14] G. García-Isla, A.L. Olivares, E. Silva, M. Nuñez-Garcia, C. Butakoff, D. Sanchez-Quintana, H.G. Morales, X. Freixa, J. Noailly, T. De Potter, O. Camara, Sensitivity analysis of geometrical parameters to study haemodynamics and thrombus formation in the left atrial appendage, Int. J. Num. Methods Biomed. Eng. 34 (2018) 1–14, https://doi.org/10.1002/cnm.3100.

[15] M. Garcia-Villalba, L. Rossini, A. Gonzalo, D. Vigneault, P. Martinez-Legazpi, O. Flores, J. Bermejo, E. McVeigh, A.M. Kahn, J.C. del Alamo, Demonstration of Patient-specific Simulations to Assess Left Atrial Appendage Thrombogenesis Risk, 2020 bioRxiv.

[16] A.S. Go, E.M. Hylek, K.A. Phillips, Y. Chang, L.E. Henault, J.V. Selby, D.E. Singer, Prevalence of diagnosed atrial fibrillation in adults, Jama 285 (2001) 2370, https://doi.org/10.1001/jama.285.18.2370.

[17] N. Gorring, L. Kark, A. Simmons, T. Barber, Determining possible thrombus sites in an extracorporeal device, using computational fluid dynamics-derived relative residence time, Comput. Methods Biomech. Biomed. Eng. 18 (2015) 628–634.

[18] H.A. Himburg, D.M. Grzybowski, A.L. Hazel, J.A. LaMack, X.M. Li, M.H. Friedman, Spatial comparison between wall shear stress measures and porcine arterial endothelial permeability, Am. J. Physiol. Heart Circ. Physiol. 286 (2004) H1916–H1922.

[19] W.K. Jeong, J.H. Choi, J.P. Son, S. Lee, M.J. Lee, Y.H. Choe, O.Y. Bang, Volume and morphology of left atrial appendage as determinants of stroke subtype in patients with atrial fibrillation, Heart Rhythm 13 (2016) 820–827, https://doi.org/10.1016/j.hrthm.2015.12.026. URL.

[20] D. Kang, J. Woo, C.C.J. Kuo, P.J. Slomka, D. Dey, G. Germano, Heart chambers and whole heart segmentation techniques: review, J. Electron. Imag. 21 (2012) 1–17, https://doi.org/10.1117/1.JEI.21.1.010901.

[21] R. Koizumi, K. Funamoto, T. Hayase, Y. Kanke, M. Shibata, Y. Shiraishi, T. Yambe, Numerical analysis of hemodynamic changes in the left atrium due to atrial fibrillation, J. Biomech. 48 (2015) 472–478, https://doi.org/10.1016/j.jbiomech.2014.12.025. URL.

[22] D.N. Ku, D.P. Giddens, C.K. Zarins, S. Glagov, Pulsatile flow and atherosclerosis in the human carotid bifurcation. positive correlation between plaque location and low oscillating shear stress, Arteriosclerosis: Off. J. Am. Heart Assoc, Inc 5 (1985) 293–302.

[23] J. Lantz, V. Gupta, L. Henriksson, M. Karlsson, A. Persson, C.J. Carlhäll, T. Ebbers, Impact of pulmonary venous inflow on cardiac flow simulations: comparison with in vivo 4D flow MRI, Ann. Biomed. Eng. 47 (2019) 413–424, https://doi.org/10.1007/s10439-018-02153-5.

[24] H. Leventić, D. Babin, L. Velickic, D. Devos, I. Galić, V. Zlokolicaf, K. Romić, A. Pizurica, Left atrial appendage segmentation from 3D CCTA images for occluder placement procedure, Comput. Biol. Med. 104 (2019) 163–174.

[25] M. Liu, J. Tilton, Spatial distributions of mean age and higher moments in steady continuous flows, AIChE J. 56 (2010) 2561–2572.

[26] J.R. López-Mínguez, J. Eldoayen-Gragera, R. González-Fernández, C. Fernández-Vegas, M.E. Fuentes-Cañamero, V. Millán-Nuñez, J.M. Nogales-Asensio, A. Martínez-Naharro, S. Sánchez-Giralt, M. Doblado-Calatrava, A. Merchán-Herrera, Resultados inmediatos y a más de un año en 35 pacientes consecutivos a los que se realiza cierre de orejuela izquierda con el dispositivo Amplatzer Cardiac Plug, Rev. Esp. Cardiol. 66 (2013) 90–97, https://doi.org/10.1016/j.recesp.2012.04.024.

[27] J.R. López-Mínguez, R. González-Fernández, C. Fernández-Vegas, V. Millán-Nuñez, M.E. Fuentes-Cañamero, J.M. Nogales-Asensio, J. Doncel-Vecino, J. Elduayen-Gragera, S.Y. Ho, D. Sánchez-Quintana, Anatomical classification of left atrial appendages in specimens applicable to CT imaging techniques for implantation of amplatzer cardiac plug, J. Cardiovasc. Electrophysiol. 25 (2014) 976–984, https://doi.org/10.1111/jce.12429.

[28] J.R. López-Mínguez, R. González-Fernández, C. Fernández-Vegas, V. Millán-Nuñez, M.E. Fuentes-Cañamero, J.M. Nogales-Asensio, J. Doncel-Vecino, M. Yuste

Domínguez, L. García Serrano, D. Sánchez Quintana, Comparison of imaging techniques to assess appendage anatomy and measurements for left atrial appendage closure device selection, J. Invasive Cardiol. 26 (2014) 462–467.

[29] J.R. López-Mínguez, J.M. Nogales-Asensio, E. Infante De Oliveira, V. De Gama Ribeiro, R. Ruiz-Salmerón, D. Arzamendi-Aizpurua, H. Costa, H. Gutiérrez-García, J.A. Fernández-Díaz, V. Martín-Yuste, J.C. Rama-Merchán, R. Moreno-Gómez, A. Benedicto-Buendía, A. Íñiguez-Romo, Long-term event reduction after left atrial appendage closure. Results of the iberian registry II, Rev. Esp. Cardiol. 72 (2019) 449–455, https://doi.org/10.1016/j.recesp.2018.03.020.

[30] A. Masci, M. Alessandrini, D. Forti, F. Menghini, L. Dedé, C. Tommasi, A. Quarteroni, C. Corsi, A patient-specific computational fluid dynamics model of the left atrium in atrial fibrillation: development and initial evaluation, in: M. Pop, G.A. Wright (Eds.), Functional Imaging and Modelling of the Heart, Springer International Publishing, Cham, 2017, pp. 392–400.

[31] A. Masci, L. Barone, L. Dedè, M. Fedele, C. Tomasi, A. Quarteroni, C. Corsi, The impact of left atrium appendage morphology on stroke risk assessment in atrial fibrillation: a computational fluid dynamics study, Front. Physiol. 9 (2019) 1–11, https://doi.org/10.3389/fphys.2018.01938.

[32] J. Mill, A.L. Olivares, X. Bijnens, X. Freixa, Optimal boundary conditions in fluid simulations for predicting occluder-related thrombus formation in the left Atria, in: 6th International Conference on Computational and Mathematical Biomedical Engineering, 2019.

[33] A. Myronenko, X. Song, Point set registration: coherent point drifts, IEEE Trans. Pattern Anal. Mach. Intell. 32 (2010) 2262–2275, https://doi.org/10.1109/TPAMI.2010.46.

[34] A.L. Olivares, E. Silva, M. Nuñez-Garcia, C. Butakoff, D. Sánchez-quintana, X. Freixa, J. Noailly, De Potter, C.O. Tom, Functional Imaging and Modelling of the Heart, Springer International Publishing AG, 2017, https://doi.org/10.1007/978-3-319-59448-4, 2017; FIMH 2017 10263, 412–420. URL, http://link.springer.com/10.1007/978-3-319-59448-4. arXiv:9780201398298.

[35] T. Otani, A. Al-Issa, A. Pourmorteza, E.R. McVeigh, S. Wada, H. Ashikaga, A computational framework for personalized blood flow analysis in the human left atrium, Ann. Biomed. Eng. 44 (2016) 3284–3294, https://doi.org/10.1007/s10439-016-1590-x.

[36] T. Otani, M. Shiga, S. Endo, S. Wada, Performance assessment of displacement-field estimation of the human left atrium from 4D-CT images using the coherent point drift algorithm, Comput. Biol. Med. 114 (2019), https://doi.org/10.1016/j.compbiomed.2019.103454.

[37] P. Peng, K. Lekadir, A. Gooya, L. Shao, S.E. Petersen, A.F. Frangi, A review of heart chamber segmentation for structural and functional analysis using cardiac magnetic resonance imaging, Magn. Reson. Mater. Phy. 29 (2016) 155–195, https://doi.org/10.1007/s10334-015-0521-4.

[38] A. Pourmorteza, K.H. Schuleri, D.A. Herzka, A.C. Lardo, E.R. McVeigh, A new method for cardiac computed tomography regional function assessment: stretch quantifier for endocardial engraved zones (SQUEEZ), Circ. Cardiovasc. Imaging 5 (2012) 243–250.

[39] D. Rueckert, L. Sonoda, C. Hayes, D.L.G. Hill, M.O. Leach, D.J. Hawkes, Nonrigid registration using free-form deformations: application to breast MR images, IEEE Trans. Med. Imag. 18 (1999) 712–721.

[40] T. Sakellaridis, M. Argiriou, C. Charitos, K. Tsakiridis, P. Zarogoulidis, N. Katsikogiannis, I. Kougioumtzi, N. Machairiotis, T. Tsiouda, S. Arikas, A. Mpakas, T. Beslevis, A. Koletas, K. Zarogoulidis, Left atrial appendage exclusion-where do we stand? J. Thorac. Dis. 6 (2014) https://doi.org/10.3978/j.issn.2072-1439.2013.10.24.

[41] S. Sankaran, H. Kim, G. Choi, C.A. Taylor, Uncertainty quantification in coronary blood flow simulations: impact of geometry, boundary conditions and blood viscosity, J. Biomech. 49 (2016) 2540–2547.

[42] G. Santoro, F. Meucci, M. Stolcova, M. Rezzaghi, F. Mori, C. Palmieri, U. Paradossi, L.E. Pastormerlo, G. Rosso, S. Berti, Percutaneous left atrial appendage occlusion in patients with non-valvular atrial fibrillation: implantation and up to four years follow-up of the AMPLATZER Cardiac Plug, EuroIntervention : J. EuroPCR Collaboration with the Working Group on Interv. Cardiol. Eur. Soc. Cardiol. 11 (2016) 1188–1194, https://doi.org/10.4244/eijy14m10_13. URL.

[43] J. Sierra-Pallares, C. Méndez, P. García-Carrascal, F. Castro, Spatial distribution of mean age and higher moments of unsteady and reactive tracers: reconstruction of residence time distributions, Appl. Math. Model. 46 (2017) 312–327.

[44] D. Spalding, A note on mean residence-times in steady flows of arbitrary complexity, Chem. Eng. Sci. 9 (1958) 74–77.

[45] S.i. Sugiyama, K. Niizuma, T. Nakayama, H. Shimizu, H. Endo, T. Inoue, M. Fujimura, M. Ohta, A. Takahashi, T. Tominaga, Relative residence time prolongation in intracranial aneurysms: a possible association with atherosclerosis, Neurosurgery 73 (2013) 767–776.

[46] A. Tzikas, S. Shakir, S. Gafoor, H. Omran, S. Berti, G. Santoro, J. Kefer, U. Landmesser, J.E. Nielsen-Kudsk, I. Cruz-Gonzalez, H. Sievert, T. Tichelbäcker, P. Kanagaratnam, F. Nietlispach, A. Aminian, F. Kasch, X. Freixa, P. Danna, M. Rezzaghi, P. Vermeersch, F. Stock, M. Stolcova, M. Costa, R. Ibrahim, W. Schillinger, B. Meier, J.W. Park, Left atrial appendage occlusion for stroke prevention in atrial fibrillation: multicentre experience with the AMPLATZER Cardiac Plug, EuroIntervention 11 (2016) 1170–1179, https://doi.org/10.4244/EIJY15M01_06.

[47] V. Vedula, R. George, L. Younes, R. Mittal, Hemodynamics in the left atrium and its effect on ventricular flow patterns, J. Biomech. Eng. 137 (2015) 1–8, https://doi.org/10.1115/1.4031487.

[48] Y. Wang, L. Di Biase, R.P. Horton, T. Nguyen, P. Morhanty, A. Natale, Left atrial appendage studied by computed tomography to help planning for appendage

closure device placement, J. Cardiovasc. Electrophysiol. 21 (2010) 973–982, https://doi.org/10.1111/j.1540-8167.2010.01814.x.

[49] A.M. Wendelboe, G.E. Raskob, Global burden of thrombosis, Circ. Res. 118 (2016) 1340–1347, https://doi.org/10.1161/CIRCRESAHA.115.306841.

[50] P.A. Wolf, R.D. Abbott, W.B. Kannel, Atrial fibrillation as an independent risk factor for stroke: the framingham study, Stroke 22 (1991) 983–988, https://doi.org/10.1161/01.STR.22.8.983.

[51] L.T. Zhang, M. Gay, Characterizing left atrial appendage functions in sinus rhythm and atrial fibrillation using computational models, J. Biomech. 41 (2008) 2515–2523, https://doi.org/10.1016/j.jbiomech.2008.05.012.